# Supporting Information

Filipov et al. 10.1073/pnas.1509465112

## SI Text

### S1) Stiffness Calculations

For our analyses and discussion in the main text, we examine the thin sheet origami in a consistent fashion to highlight the behaviors, while staying independent of scale (eigenvalue and static analyses). The eigenvalues ($\lambda$) have units of $1/s^2$ and represent the global characteristics of the structure considering both mass and stiffness. The static analyses present the global structural stiffness in the form of force divided by displacement. The two different computational models used herein (bar and hinge model and finite elements) give similar results and correspond well with observations of physical models.

For our analyses we use the following parameters unless otherwise noted. The Miura-ori sheet (Fig. 2*B*) with unit dimensions $a=c=1$, $\alpha=55°$, and $N=5$ is used to define the tubes and coupled tube systems used in the analyses of Figs. 3 and 4 (see *SI Text*, section S5 for additional details on internally coupled tubes). A Miura-ori sheet with $a=c=1$, $\alpha=75°$, and $N=3$ is used for the cellular assemblage in Fig. 5. The thickness $t=0.01$ is used to simulate a thin sheet that is much thinner than it is long ($L/t=100$). A Young's modulus $E=10^6$ and material density $\rho=1$, both arbitrary but within a realistic range, are selected to scale stiffness and mass linearly and do not affect the global behavior or characteristics of the origami tubes (Fig. S4 and accompanying discussion). The elastic modulus is assumed to be in units of force per length squared (e.g., newtons per square millimeter) and the density as mass per length cubed (e.g., kilograms per cubic millimeter). When appropriate numerical values and length scales are used, the analyses presented here will provide quantitative approximations for stiffness and eigenvalue response. Other parameters used in the modeling are discussed in the text below and are chosen based on existing literature, approximate physical behavior, and type of computation performed (e.g., Poisson's ratio $\nu=1/4$).

Here, we describe the simple bar and hinge method for the numerical modeling of thin sheets in origami systems. A previously established model (24) is used as a basis, and several improvements are incorporated to make the model scalable and isotropic and to incorporate material characteristics (32). We make the stiffness dependent on the material's thickness ($t$), Young's modulus ($E$), and Poisson's ratio ($\nu$). The stiffness matrix ($\mathbf{K}$) for the origami structure incorporates stiffness parameters for (*i*) panels stretching and shearing ($\mathbf{K}_S$), (*ii*) panels bending ($\mathbf{K}_B$), and (*iii*) bending along prescribed fold lines ($\mathbf{K}_F$). The global stiffness matrix is constructed as

$$\mathbf{K}=\begin{bmatrix}\mathbf{C}\\ \mathbf{J}_B\\ \mathbf{J}_F\end{bmatrix}^{\mathrm{T}}\begin{bmatrix}\mathbf{K}_S & \mathbf{0} & \mathbf{0}\\ \mathbf{0} & \mathbf{K}_B & \mathbf{0}\\ \mathbf{0} & \mathbf{0} & \mathbf{K}_F\end{bmatrix}\begin{bmatrix}\mathbf{C}\\ \mathbf{J}_B\\ \mathbf{J}_F\end{bmatrix}, \qquad [S1]$$

where the compatibility matrix ($\mathbf{C}$) and Jacobian matrices ($\mathbf{J}_B$ and $\mathbf{J}_F$) relate the stiffness of the various components to the nodal displacements, as discussed in detail below. Each node has 3 degrees of freedom (DOFs) ($X$, $Y$, and $Z$ displacement) and the stiffness matrix is of size ($n_{\mathrm{dof}}\times n_{\mathrm{dof}}$), where $n_{\mathrm{dof}}$ represents the total number of DOFs in the system. The mass of each panel is calculated from the panel volume and material density $\rho$. A mass matrix $\mathbf{M}$ for the entire structure is constructed by distributing one-quarter of the mass of each panel to each of its connecting nodes.

**S1.1) Panel Stretching and Shearing.** In-plane axial and shear stiffness is simulated using the indeterminate bar frame (Fig. S1*A*). A general formulation for bar elements is used with an equilibrium matrix ($\mathbf{A}$) relating internal bar forces ($\mathbf{t}$) to nodal forces ($\mathbf{f}$) as $\mathbf{At}=\mathbf{f}$, a compatibility matrix ($\mathbf{C}$) relating bar nodal displacements ($\mathbf{d}$) to bar extensions ($\mathbf{e}$) as $\mathbf{Cd}=\mathbf{e}$, and a diagonal matrix ($\mathbf{K}_S$) relating bar extensions ($\mathbf{e}$) to local forces ($\mathbf{t}$) as $\mathbf{K}_S\mathbf{e}=\mathbf{t}$. Using the static-kinematic duality that $\mathbf{C}=\mathbf{A}^T$, the linear system for stretching and shear of the panels (i.e., the bars) is represented as the first row of Eq. **S1**. The crossed bar frame (Fig. S1*A*) has six bars connected at the four corner nodes of the origami panel. This crossed bar geometry results in the frame behaving as an isotropic panel. The bar stiffness parameters (i.e., components of $\mathbf{K}_S$) are defined for each bar as $K_S=EA_B/L_B$, where $L_B$ is the bar length and $A_B$ is the bar area. To achieve the isotropic behavior for the panel, the bar areas are defined as

$$A_X=t\frac{H^2-\nu W^2}{2H(1-\nu^2)}, \qquad [S2]$$

$$A_Y=t\frac{W^2-\nu H^2}{2W(1-\nu^2)}, \qquad [S3]$$

$$A_D=t\frac{\nu\left(H^2+W^2\right)^{3/2}}{2HW(1-\nu^2)}, \qquad [S4]$$

for the horizontal ($X$), vertical ($Y$), and diagonal ($D$) bars, respectively. The height ($H$) and width ($W$) of the panel are taken as an average for skewed panels. To verify the frame model we define a panel with $W=H=1$, $t=0.01$, $E=1{,}000$, and $\nu=1/3$ and subject it to a tensile (Fig. S1*B*) and a shear patch test (Fig. S1*C*). For tensile loading the system always satisfies the patch test, but for shear loading, the behavior of the model is highly dependent on the chosen Poisson's ratio. From Eq. **S4**, when a low $\nu$ is used, the diagonal bars have a low area, and the frame demonstrates a low shear stiffness. The converse is also true, countering the behavior expected in a truly isotropic material. Alternatively, when $\nu$ is set to $1/3$, the behavior of the frame model in shear is identical to that of a homogeneous, isotropic block of material. Each diagonal bar carries a force of $F/2$ in the $X$ direction, and the top of the frame laterally displaces in the direction of loading. When $\nu=1/3$, the frame displacement matches the lateral displacement of a solid block with dimensions $W\times H\times t$ loaded in pure shear, analytically defined as $\Delta_x=F_XH/GWt$, where $F_X$ is the total shear force and $G$ is the shear modulus, defined as $G=E/2(1+\nu)$ for a homogeneous, isotropic, linear elastic material. With $\nu=1/3$, the frame is scale independent for shear loadings. If the shear patch is remeshed, then the frame model converges to the same solution as any generic finite-element approach. However, because only a single six-bar frame is used to model each panel, the shear stiffness of the panel is overestimated (similarly to any finite-element approach). In reality, the shear stiffness of the panels is lower than a pure shear case because, in addition to the shear deformations, tensile deformations also occur over the width and height of the panel. Using a lower Poisson's ratio, we artificially reduce the shear stiffness of the frame. To this end, we choose to use $\nu=1/4$. At this value, the single bar frame exhibits approximately the same shear deformation as a patch test performed on a mesh of 2,500 finite elements.

**S1.2) Panel Bending.** Out-of-plane bending of the panel is modeled as an angular constraint between two triangular segments of the panel (1–2–3 and 1–3–4 in Fig. S1*D*). For small displacements, the choice of the diagonal does not affect the kinematics of the system (7). Previous findings (1, 4) show that the bending energy is lower along the shorter length, so we formulate our model assuming that bending occurs along the shorter diagonal (i.e., 1–3 in Fig. S1*D*). An angular constraint, $F$, is formulated based on the dihedral bending angle, $\theta$, which can be calculated by using cross and inner products of the vectors **a**, **b**, and **c** from the nodal coordinates of the panel **p**. This constraint is defined as

$$F = \sin(\theta(\mathbf{p})), \qquad \textbf{[S5]}$$

and the corresponding Jacobian for panel bending, $\mathbf{J}_B$, is calculated as

$$d\theta = \frac{1}{\cos(\theta)} \sum \frac{\partial F}{\partial p_i} dp_i = \mathbf{J}_B \mathbf{d}, \qquad \textbf{[S6]}$$

where **d** are the displacements of the panel nodes. The second row of Eq. **S1** incorporates panel bending stiffness where each element in the diagonal matrix $\mathbf{K}_B$ corresponds to the bending stiffness of an individual panel.

We assume that the in-plane stiffness of the thin sheet (e.g., paper) is high enough to prevent bending and buckling at the edge connecting two panels (i.e., at the fold line of a thin sheet). The bending energy of thin sheets increases when the edges of the sheet are restrained. In this case, tensile forces develop over the sheet's surface, and flexural deformations become restricted to a small area focused at the bending ridge (i.e., the diagonal 1–3 in Fig. S1 *D*–*F*) (1, 2, 4). This phenomenon occurs with large displacements and the elastic energy of the panel bending scales approximately as $k(L_2/t)^{1/3}$, where $k$ is the bending modulus of the sheet, defined as $k = Et^3/12(1-\nu^2)$ (1). In our model we define the panel stiffness as

$$K_B = C_B \frac{Et^3}{12(1-\nu^2)} \left(\frac{L_2}{t}\right)^{1/3}, \qquad \textbf{[S7]}$$

which incorporates the nonlinear effect of the $L_2/t$ ratio in the restricted bending of a thin sheet. We use a finite-element model (discussed in detail later) to show thin sheet bending for small and for large displacement cases. We define a thin sheet with a long diagonal $L_1 = 1$ and a short diagonal of $L_2 = 0.8$. The thin panel is restrained at the edges by thin sheets in a perpendicular orientation (similar to typical origami). The structure is restrained in the vertical direction at three corners and is subjected to bending with a downward force $F$ at the fourth corner (Fig. S1*E*). When a small force is applied ($F = 0.01$), the structure remains in the small displacement regime and the thin sheet experiences curvature along both diagonals (Fig. S1*F*, *Top*). For a larger force ($F = 1.0$) the structure experiences large displacements, and curvature occurs in the center of the $L_1$ diagonal, creating a bending ridge along the $L_2$ diagonal (Fig. S1*F*, *Bottom*). As discussed in previous literature (1, 4) the large displacement case has a higher stiffness and the rotational hinge formulation in Eq. **S7** would give a realistic result with a factor of $C_B = 0.794$. Here we restrict ourselves to small displacements, and so we use $C_B = 0.441$ for all analyses. The stiffness coefficient $C_B$ has not been investigated in detail yet. A more comprehensive formulation would incorporate a nonlinear scaling associated with the dihedral bending angle $\theta$ into Eq. **S7** that would scale stiffness between small and large displacement cases. For example, ref. 1 suggests that the total bending energy (and thus stiffness) of the restricted sheet should scale with $\theta^{7/3}$ vs. $\theta^2$ for a linear rotational hinge.

**S1.3) Folds Bending.** Folds are modeled in a similar fashion to the bending of panels. Realistic origami behavior does not allow for out-of-plane displacements along fold lines due to the restrictive nature of the perpendicularly oriented sheets. Thus, it is sufficient to use a simplified approach: modeling the origami fold as a rotational hinge along an edge. A schematic of the fold model contains a fold spanning nodes 2 and 3 connecting two panels (1–2–3–4 and 2–5–6–3) (Fig. S1*G*). The length of the fold is $L_F$, and the stiffness is expected to scale linearly with this length, because curvature and bending energy are expected to exist only on the infinitesimally small width of the fold. The same constraint formulation presented for the panel bending is used to formulate two independent fold elements from the two vector sets: (*i*) **a**, **b**, and **c** and (*ii*) **−a**, **d**, and **e**. This approach distributes the stiffness of the fold to all relevant nodes on the two adjacent panel elements. The initial fold angle, $\theta_0$, is different for different folds on the Miura-ori sheet and tube and can be calculated using basic geometric relations (7, 25, 27) for each chosen configuration (percentage of extension). Here, the angle $\theta$ represents a rotation away from the initial folded configuration.

We introduce a parameter $R_{FP}$ to relate the stiffness between the bending of a fold with length $L_F = 1$ and the bending of a panel with a diagonal of $L_2 = 1$. Structures consisting of thick panels with near frictionless hinges (18, 19) could have a low $R_{FP}$ (e.g., $10^{-4}$); structures where perforation or plastic deformation is used to facilitate creasing (34, 35) could have a medium $R_{FP}$ (e.g., 0.1); whereas origami created with additive manufacturing (40), or where creasing is near elastic (36), could have a $R_{FP} = 1$ and perhaps higher if movement at folds is intentionally restricted. The interaction between bending of flat material and folding at fold lines as well as highly nonlinear folding behaviors of origami are currently being studied (33–36). Our simplifications assume that only linear elastic deformations occur at the folds. For the analyses in Figs. 3 and 4 and *SI Text*, we assume that the folds are less stiff than the panels, and we use an arbitrary choice of $R_{FP} = 1/10$ based on visual observations of our physical models. For the cellular assemblage in Fig. 5, we use $R_{FP} = 1$ to simulate folds that are as stiff as the panels, because this is likely the case for continuous 3D printed structures. In *SI Text*, section S3 we show that $R_{FP}$ influences the magnitude of eigenvalues associated with fold bending; however, it does not influence the overall behavior and the qualitative results presented in this paper. For our implementation, the stiffness for each of the twofold elements (i.e., **a**, **b**, **c** and **−a**, **d**, **e**) is calculated similarly to Eq. **S7**, as

$$K_F = R_{FP} \frac{L_F}{2} C_B \frac{Et^3}{12(1-\nu^2)} \left(\frac{1}{t}\right)^{1/3}, \qquad \textbf{[S8]}$$

except here the function scales linearly with the length $L_F$. More comprehensive future formulations may incorporate nonlinear scaling associated with material properties, the angle $\theta$, the angle $\theta_0$, and other fold-related variables (33–36).

## S2) Coupling of Zipper Tube Structures

In the computer model, the coupling of the zipper structures is performed by inserting coupling elements that restrict relative movement between the adjacent panels of the two tubes. These coupling elements can be thought of as an adhesive joint between the adjacent faces of the tube. The relative local coordinates ($X'$ and $Z'$) are different for the odd and even panels of the structure (Fig. S2). The $X'$ coupling elements restrain relative movement between panels along the length of the tube (relative to the local $X'$ axes), and the $Y'$ coupling elements restrain differential orthogonal movement in the $Y'(=Y)$ axis. The $X'$ and $Y'$ coupling elements are formulated using a compatibility relation where bar

elements are used to restrain relative movement between two nodes. The stiffness for the coupling elements is defined as

$$K_{X'} = C_{X'}\frac{EA}{L} = C_{X'}\frac{E0.5t}{1}, \quad \textbf{[S9]}$$

and

$$K_{Y'} = C_{Y'}\frac{EA}{L} = C_{Y'}\frac{E0.5t}{1}, \quad \textbf{[S10]}$$

where $E$ is Young's modulus, $t$ is the thickness of the thin sheet, and the coupling coefficients ($C_{X'}$ and $C_{Y'}$) can be used to vary the stiffness of the coupling elements. When these coupling coefficients are set to 1, each coupling element has the same axial stiffness as a 0.5-unit-wide, 1-unit-long, and $t$-thick piece of panel material. Finally, $Z'$ coupling elements are used to prevent nodes lying on the same plane (on a panel) from moving out-of-plane (in the relative $Z'$ direction). The $Z'$ coupling elements are defined in the same fashion as the out-of-plane rotational hinges for panel and fold bending. Here, we consider a node on one of the zipper tubes that overlaps a panel on the opposite tube, indicated as a red/white triangle in Fig. S2*C*. A rotational hinge element is constructed that restricts out-of-plane movement between each of the overlapping nodes and the three corresponding nodes on the opposing tube. For clarity, only two sample corresponding node sets are illustrated in Fig. S2*C*. The vectors groups (**a**, **b**, and **c**) and (**d**, **e**, and **f**) can be used to define the rotational hinge for each set. The stiffness for each of these rotational hinges is defined as

$$K_{Z'} = C_{Z'}C_B\frac{Et^3}{12(1-\nu^2)}\left(\frac{1}{t}\right)^{1/3}, \quad \textbf{[S11]}$$

where the parameters are the same as the panel definition in Eq. **S7**, and the coupling coefficient $C_{Z'}$ can be used to vary the stiffness of the coupling elements. With this formulation, the stiffness of each $Z'$ coupling element is equal to the bending stiffness of a panel element with a diagonal length, $L_2 = 1$. Because the equation for $K_{Z'}$ is based on bending of the thin sheet, the value of this stiffness is substantially lower than that of the $X'$ and $Y'$ coupling elements.

The sensitivity of the model eigenvalues vs. the magnitude of each of the coupling coefficients is explored for the zipper-coupled tubes deployed to 70% extension (Fig. S2). The rigid folding mode ($\lambda_7$) of the coupled tube is not affected by any of the coupling elements; i.e., it is neither easier nor harder to fold and unfold the structure due to the coupling. When the coupling coefficient $C_{X'}$ is substantially reduced (lower than $10^{-2}$), the eighth and subsequent eigenvalues experience a drop in magnitude from ~1,200 to ~500. This drop occurs because the tubes are not restrained in the relative $X'$ direction, and thus the eighth mode switches to a deformation mode in which the tubes begin to separate. Due to the presence of the $Z'$ coupling elements, the magnitude of this eigenvalue remains relatively high even when $C_{X'} = 10^{-5}$ ($\lambda_8 = 560$ vs. $\lambda_8 = 20.7$ for a single tube). When decreasing the value of the $C_{Y'}$ coupling coefficient, there is a more significant effect on $\lambda_8$ and the subsequent eigenvalues. The eigenvalue corresponding to bending reduces to $\lambda_8 = 590$, when $C_{Y'} = 10^{-3}$, and experiences a mode switch for lower coupling coefficients. When $C_{Y'}$ is substantially reduced, the tubes are free to slide apart in the $Y$ direction. The $C_{Z'}$ coupling coefficients, on the other hand, have no influence on any of the eigenvalues. This is due to the zig-zag geometry of the tubes, which causes the axial members to restrain global out-of-plane movement between the two tubes. When any of the coupling coefficients are increased past a value of 1, there is negligible increase in the eighth and subsequent eigenvalues of the structure.

When changing the value of the vertex angle $\alpha$ or the extended configuration of the zipper-coupled tubes, there is little change in the sensitivity of the different coupling elements, and the general trends remain. The tubes are effectively coupled when the coupling coefficients are about equal to 1. The $X'$ and $Y'$ coupling elements have a higher influence on the coupling and on maintaining the relatively large bandgap ($\beta = \lambda_8 - \lambda_7$), whereas the $Z'$ coupling elements have little influence on the eigenvalues.

To better understand why the zipper coupling results in the large bandgap increase, we investigate how the squeezing deformation mode is restrained by the new geometry. We perform an eigenvalue analysis on two tubes arranged in a zipper-coupling fashion, when the stiffness of all coupling elements is substantially reduced ($C_{X'} = C_{Y'} = C_{Z'} = 0.0005$). In this scenario the tubes can simultaneously undergo the squeezing deformation mode, where the tubes fold on the left side and unfold on the right (Fig. S3 *A*–*C*). However, this motion is incompatible for an effectively coupled zipper system. On the left side, the first vertex of the bottom tube moves downward (point I in Fig. S3*A*), whereas the first vertex on the top tube moves upward (point II in Fig. S3*B*) and vice versa on the right side. This transverse motion between the two tubes can be quantified by tracking the distance between adjacent panel-edge center points on the two tubes (Fig. S3*D*). In an undeformed (or effectively coupled) system the distance between adjacent edge center points is uniform at 0.7 units. The squeezing of the loosely coupled system results in separation on the left side (distance increases up to 0.9 units) and a closing on the right side (distance decrease down to 0.5 units). In an effectively coupled zipper system these in-plane motions are restrained, and it would be necessary to stretch and shear the thin sheet to achieve a squeezing-type deformation.

### S3) Sensitivity of Model and Analysis

In Fig. S4 we show differences in scaling of eigenvalues, for the tube and zipper-coupled tubes, with respect to different model parameters. The seventh eigenvalue for both the single tube and the zipper-coupled tubes corresponds to the rigid folding mode, in which deformation primarily occurs as bending of the prescribed folds (Fig. 3 and Fig. S7). The eighth mode for the single tube corresponds to squeezing, in which bending occurs in the fold and panel elements. However, the eighth mode for the zipper-coupled tubes requires stretching and shearing of the thin sheet, which require much more energy than bending and result in drastic differences for the scaling of eigenvalues.

All eigenvalues ($\lambda_7$ and $\lambda_8$ for both systems) scale proportionally with Young's modulus $E$ (i.e., doubling $E$ doubles the eigenvalue) and inversely proportionally with the material density $\rho$ (Fig. S4 *A*, *B*, *E*, and *F*). This is expected because $E$ scales the stiffness proportionally, and $\rho$ scales the mass proportionally in equation $\mathbf{K}v_i = \lambda_i\mathbf{M}v_i$. Scaling of other parameters, however, does not necessarily influence all eigenvalues proportionally. When changing the sheet's thickness, $t$, its stretching/shearing stiffness and the system's mass scale proportionally. On the other hand, the bending stiffness for both the panels and the folds scales as $8/3$ based on Eqs. **S7** and **S8**. Therefore, when scaling the thickness, the eigenvalues scale as $5/3$ for the rigid folding modes ($\lambda_7$) of both tubes, and the squeezing mode ($\lambda_8$) of the single tube (Fig. S4 *C* and *G*). The eighth eigenvalue for the zipper-coupled tubes does not change because both mass and stretching/shear stiffness scale proportionally (both are defined by $t$). When scaling the fold stiffness ratio, $R_{FP}$, $\lambda_7$ scales proportionally for both structures, $\lambda_8$ scales as 0.8 for the single tube, and $\lambda_8$ remains constant for the zipper tubes (Fig. S4 *D* and *H*). The system behaviors that lead to these scaling relations are complemented by the energy distributions shown in Fig. S7.

In summary, Young's Modulus $E$ and material density $\rho$ directly scale all system eigenvalues, whereas the material thickness $t$ and fold stiffness ratio $R_{FP}$ scale eigenvalues influenced by panel and fold bending. The scaling of different parameters does not cause mode switching and the order of eigenmodes remains the same as shown in Fig. 3. Scaling different parameters can change the quantitative results (e.g., magnitude of $\lambda_7$); however, it does not influence the qualitative results presented here. The eighth eigenvalue for the zipper-coupled tubes remains substantially higher than the seventh, ensuring a large bandgap ($\beta = \lambda_8 - \lambda_7$) regardless of the parameter values used. The results presented in this paper are independent of length scale, making the zipper-coupled tubes applicable across scales.

### S4) Model Verification with Finite-Element Analysis

In this section, we verify and explore the accuracy of the bar and hinge model by comparing the results from the bar and hinge model to those of a shell model created using the commercial finite-element (FE) analysis software ABAQUS (41). Details of the FE implementation are shown in Fig. S5*A* for a single Miura-ori cell. For the FE model, we discretize each panel into $D$ segments in each direction, such that each panel will now be modeled using $D^2$ shell elements ($D = 8$ for Fig. S5*B* and for all FE analyses herein). General purpose, four-node shell elements with finite membrane strains are used (S4 elements) and are connected with one node at each corner. The fully 3D FE model contains 6 DOFs at each node (3 displacements and 3 rotations). Mass in the model is distributed based on the volume and the density, $\rho$, of the shell elements. All model parameters are defined to be the same as those for the bar and hinge model.

At the fold lines, collocated (overlapping) nodes are placed with one node connected to the shell elements of each adjoining panel. Each set of collocated nodes, shown in Fig. S5*A*, *Inset*, is connected with an element that restricts the nodes to the same *XYZ* coordinates throughout the analysis. At the same location, the fold stiffness is modeled as an elastic rotational spring that resists rotation between the adjacent panels. The spring is placed locally on each pair of collocated nodes and resists rotations about the local **a** vector shown in Fig. S5*A*, *Inset*. The stiffness of the fold is based on the dimensions of connected shell elements and is defined as

$$(K_F)_{FE} = \frac{(L_{S1} + L_{S2})/2}{L_F} K_F(L_F), \qquad \textbf{[S12]}$$

where $L_{S1}$ and $L_{S2}$ are the lengths of the connected shell element parallel to the fold line. The parameter $L_F$ denotes the length of the entire fold, and the equation $K_F$ is a function of stiffness (i.e., Eq. **S8**) based on the fold length and the same material properties as before. Eq. **S12** distributes the stiffness of the fold (as calculated for the bar and hinge model) based on the tributary length of the shell elements used. Collocated nodes that are at the end of a fold (i.e., at a vertex) will have only one adjacent shell element and thus the stiffness will be based only on $L_{S1}/2$ or on $L_{S2}/2$.

Discretized FE models of the sheet, the single tube, and zipper-coupled tubes are created with $D = 8$ and a natural eigenvalue extraction is performed. The eigenvalue spectra calculated with the FE model and the bar and hinge model are presented in Fig. S6. The seventh through ninth eigenmodes for the FE model match those of the bar and hinge model when considering the global deformation of the structure (Fig. 3 *D–F* and Fig. S6 *D–F*), which we expect because these deformation modes correspond to global behaviors of the structure such as bending and rigid folding. The magnitudes of the eigenvalues follow similar trends between the two models but do not always match exactly. For example, with the single tube, $\lambda_7$ and $\lambda_8$ match well because the fold stiffness between the two models is the same (i.e., Eqs. **S8** and **S12**), and in the FE model, panel bending occurs globally on the diagonal (as predicted for Eq. **S7**). However, the magnitude of the eigenvalues $\lambda_9$ and $\lambda_{10}$ for the tube is lower with the FE model. The difference in magnitude can be attributed to the localized deformations and stress concentrations that can be captured with the FE discretization, but cannot be captured using the bar and hinge model. For example, in the ninth mode the Miura-ori cell in the middle of the tube experiences bending, stretching, and shear localized at the vertex. The FE model can capture localized effects and individual shell elements can deform more than others. On the other hand, in the bar and hinge model stretching, shear, and bending can be captured globally only over the entire panel.

We also use the FE model to perform energy analyses for the Miura-ori sheet, the single tube, and the zipper-coupled tubes (Fig. S7). The energies are calculated based on the structural deformation for the normalized mode shapes (Fig. S6 *D–F*). The percentage of distribution between the different sets of element deformations (i.e., fold bending, panel bending, and panel stretching/shear) and the total energy for each mode are shown. The total energy for eigenvalues of the single sheet is relatively low, because deformations consist of localized bending in panels and folds. On the other hand, the eighth and ninth modes of the zipper-coupled tubes require much more energy, because the thin sheets are engaged in stretching and shearing. The rigid folding modes, ninth for the sheet and seventh for the tube structures, primarily engage the fold lines in bending as previously expected.

### S5) Aligned and Internally Coupled Tubes

The eigenvalue vs. configuration plots and representative eigenmodes at 70% extension are illustrated for the aligned-, internally, and zipper-coupled tubes in Fig. S8. The aligned-coupled tubes are constructed by translating a tube and attaching it to the initial tube without rotation (Fig. 2*E*). The tube could be a copy of the original geometry or could have different parameters $a$ and/or $\alpha$. For internally coupled tubes, the geometries of the internal and external tubes have to conform to preserve flat and rigid foldability as discussed in ref. 7. Here, we define the internal tube geometry, using a parameter $I_{\text{Ext}}$ that describes the maximum extension of the internal tube with respect to the external tube. For example, if we take an internal tube defined with $I_{\text{Ext}} = 0.8$, then the internal tube will reach 100% extension (lie flat in the $X - Y$) plane, when the external tube reaches 80% of its maximum extension. The internal tube geometry ($a_I$, $c_I$, and $\alpha_I$) is calculated from

$$a_I = \frac{a\cos(\alpha)}{\sqrt{1 - (I_{\text{Ext}})^2 \sin(\alpha)^2}}, \qquad c_I = I_{\text{Ext}} c, \qquad \textbf{[S13]}$$

and

$$\alpha_I = \sin^{-1}(I_{\text{Ext}} \sin(\alpha)), \qquad \textbf{[S14]}$$

where $a$, $c$, and $\alpha$ define the external tube geometry. The internally coupled tubes discussed in this paper (Figs. 2*F* and 4 and Figs. S8 and S9) use $I_{\text{Ext}} = 0.8$ and the conforming Miura-ori cell geometry is therefore $a_I = 0.759$, $c_I = 0.8$, and $\alpha_I = 40.94°$. Computational modeling of the connectivity required to create aligned and internally coupled tubes is much simpler to formulate than that of the zipper-coupled tubes. Nodes on adjacent faces and edges of each tube are conveniently located at the same coordinates; therefore, the same DOFs are used for both tubes, and only one of the colocated nodes is used in the model.

This modeling approach effectively connects the two systems but provides more stiffness than the coupling element approach used for the zipper-coupled tubes.

The eigenvalues $\lambda_7$ and $\lambda_8$ for the aligned-coupled tubes (Fig. S8A) are almost identical to those of the single tube (Fig. 3*B*), because coupling tubes in this fashion doubles the system's mass, and simultaneously adding an identical set of elements to the system doubles the stiffness. The seventh and eighth mode shapes are identical to the single tube and are not restricted by this form of coupling (Fig. 3*E* and Fig. S8D). The magnitude of the ninth eigenvalue increases slightly, which can be attributed to the aligned coupling.

Coupling tubes internally (Fig. 2*F*) has more of an effect on their behavior; however, $\lambda_7$ and $\lambda_8$ still correspond to the rigid folding and squeezing modes, respectively, and the bandgap is not substantially increased (Fig. S8 *B* and *E*). When approaching an extension of 80% (with respect to the external tube), the internal tube becomes flat, and the system essentially locks. At these larger extensions (60–80%), the eigenvalues $\lambda_7$ and $\lambda_8$ increase significantly, meaning that the system is substantially stiffer. When the internal tube is flattened, folding the structure (rigid folding mode) or deforming it in any other mode becomes more difficult. With other coupling orientations (i.e., zipper or aligned), the eigenvalues drop rapidly at large extensions. In those cases, the entire structure becomes essentially flat (in the $X - Y$ plane), and it becomes easy to bend the system out-of-plane. In contrast to the zipper-coupled tubes, neither the aligned-coupled tubes nor the internally coupled tubes show a substantial increase in the bandgap ($\beta = \lambda_8 - \lambda_7$) (Fig. S8 *A*–*C*). However, multiple coupling orientations can be integrated into a single system to take advantage of the different behaviors. For example, a combined zipper-coupled and internally coupled system would not experience squeezing and it would lock at a specified configuration.

### S6) Self-Interlocking Structure

Each side of the self-interlocking structure (Fig. 6*C*) can be composed of any number of zipper-coupled tubes together (of same $\alpha$). The structure can be any radially symmetric shape with $n$ sides, as long as there is no self-intersection. The structure will interlock when an angle ($\gamma$) between the two faces on the $Y - Z$ cross section of the Miura-ori cell is at $\gamma = 360°/n$. Thus, the structure will interlock at an extension of

$$\text{Ext} = 100\% \frac{\sqrt{1 - \cos(\gamma/2)^2 \big/ \sin(\alpha)^2}}{\sin(\gamma/2)}. \qquad \textbf{[S15]}$$

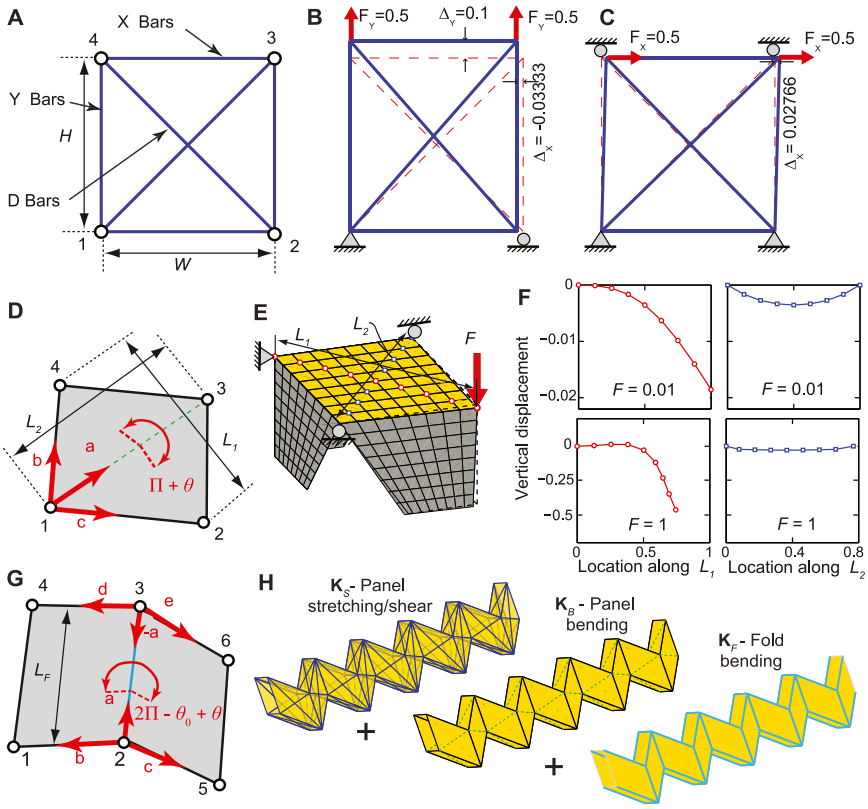


**Fig. S1.** Schematics and tests of the bar and hinge model. (*A*) Schematic of indeterminate bar frame for simulating in-plane panel stretching and shearing. (*B*) Tensile patch test of bar frame exhibiting isotropic behavior. (*C*) Shear patch test of bar frame. (*D*) Schematic orientation of rotational hinge simulating panel bending along the diagonal $L_2$. (*E*) FE model used to study bending of thin sheet restrained at edges by orthogonally placed thin sheets. (*F*) Curvature along the diagonals of the FE model for a small displacement ($F = 0.01$) and a large displacement ($F = 1$) case. (*G*) Schematic of the two rotational hinges used to simulate bending along a prescribed fold line of length $L_F$. (*H*) The three components of the bar and hinge model shown on the single tube.

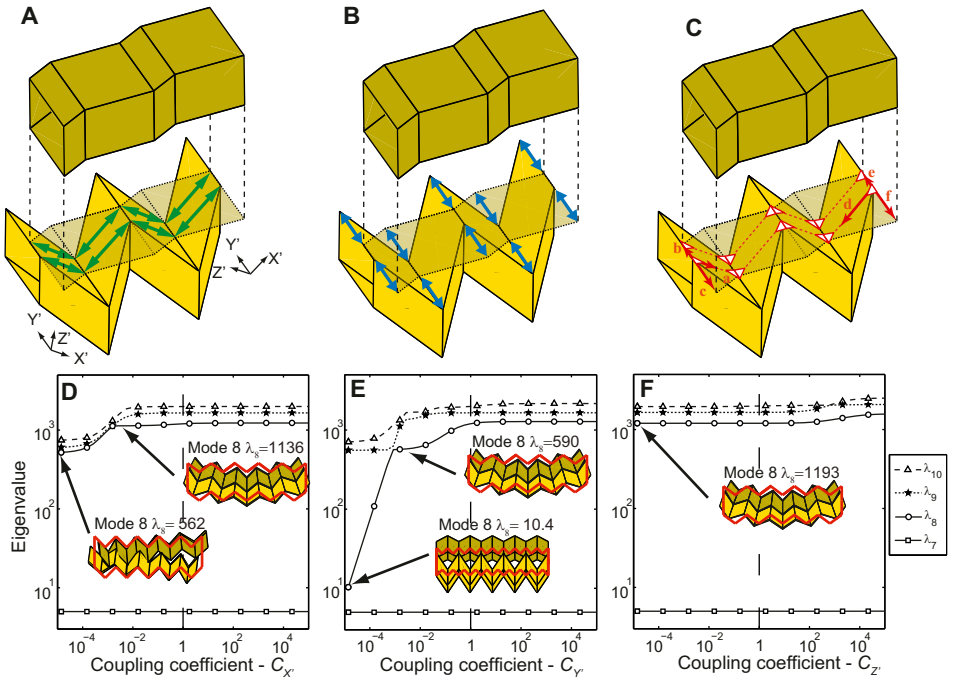


**Fig. S2.** Coupling elements used to connect zipper tubes in the bar and hinge model. (*A*–*C*) Configuration of $X'$, $Y'$, and $Z'$ coupling elements, respectively, for a segment of zipper-coupled tubes. The local axes are shown for the leftmost and rightmost panels of *A*. Only representative coupling elements are shown for the $Z'$ coupling. (*D*–*F*) The sensitivity of the system eigenvalues vs. magnitude of each of the coupling coefficients $C_{X'}$, $C_{Y'}$, and $C_{Z'}$, respectively, when the other coupling coefficients remain at a value of 1.

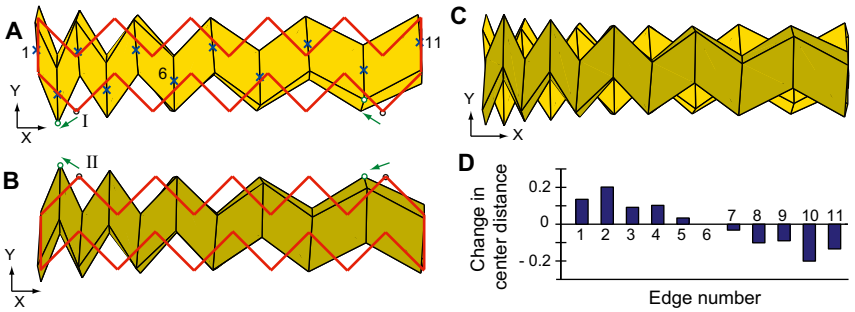


**Fig. S3.** Squeezing deformation of zipper-coupled tubes when the coupling coefficients are reduced to $C_{X'} = C_{Y'} = C_{Z'} = 0.0005$. (*A*) Top view of only the deformed bottom tube with an outline of its initial configuration. The x marks indicate the panel-edge center points on the side of the tube that is attached. (*B*) Only the deformed top tube. (*C*) The squeezing deformation of the zipper-coupled assembly with low coupling. (*D*) Change in the distance between the panel-edge center points of the two tubes. Initial distance before deformation is 0.7 units for all locations; the squeezing results in separation on the left side and closing on the right side of the coupled tubes.

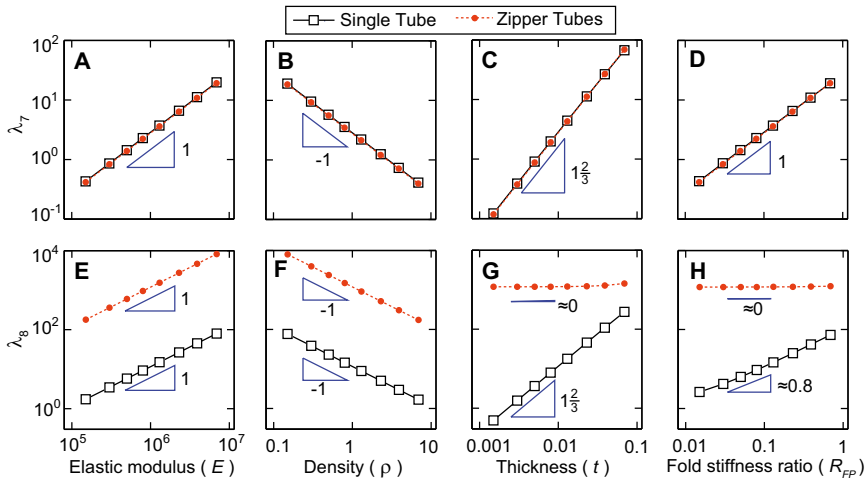


**Fig. S4.** Eigenvalue sensitivity for a single tube and the zipper-coupled tubes. (*A*–*D*) Scaling of $\lambda_7$ with respect to $E$, $\rho$, $t$, and $R_{FP}$. (*E*–*H*) Scaling of $\lambda_8$ for the same cases. These relations directly govern the scaling sensitivity of the bandgap.

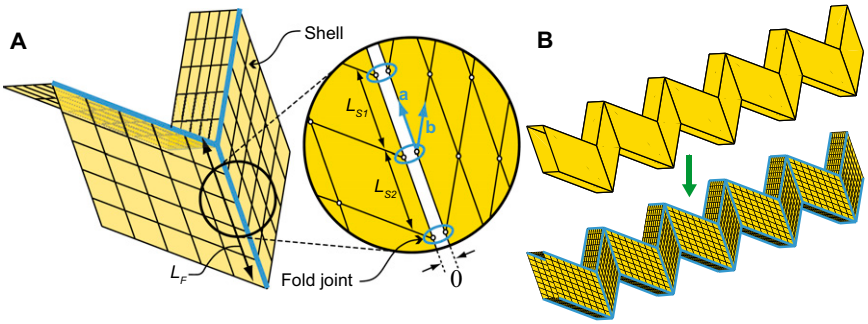


**Fig. S5.** FE model used for verification. (*A*) Miura-ori cell discretized with $D = 5$ elements for each panel; *Inset* shows local zero-length connectivity at fold lines. (*B*) Discretization of single tube with $D = 8$.

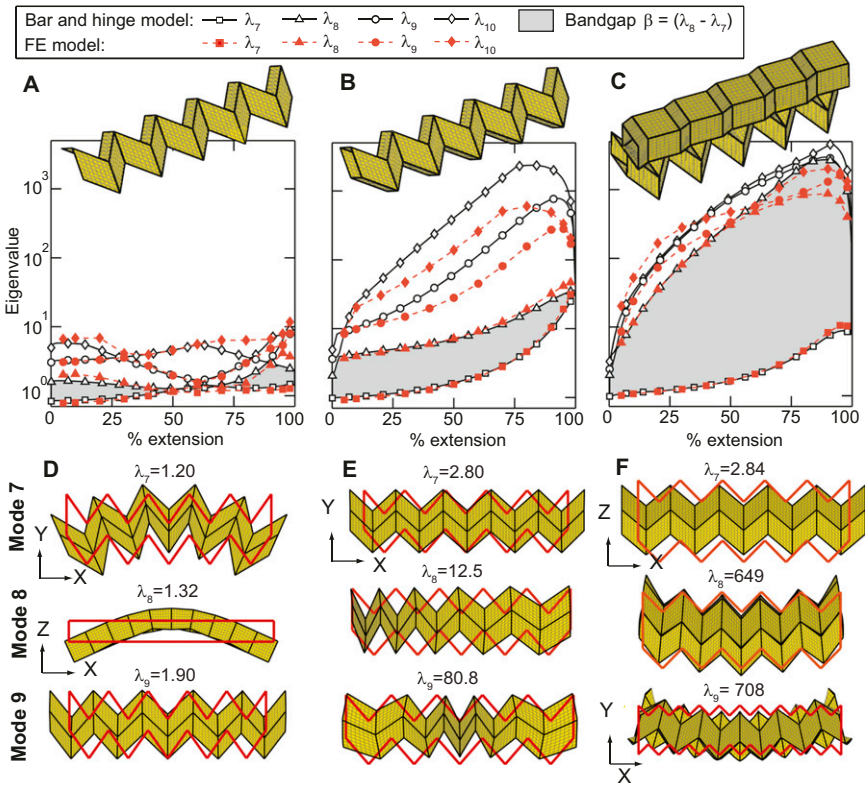


**Fig. S6.** Eigenvalue analyses of a sheet, a single tube, and a zipper-coupled tube performed with the FE model. (*A*–*C*) Eigenvalue vs. extension for the three structures, performed with both the FE and the bar and hinge models. (*D*–*F*) Seventh, eighth, and ninth deformation eigenmodes when structures are at 70% extension (undeformed outline in red).

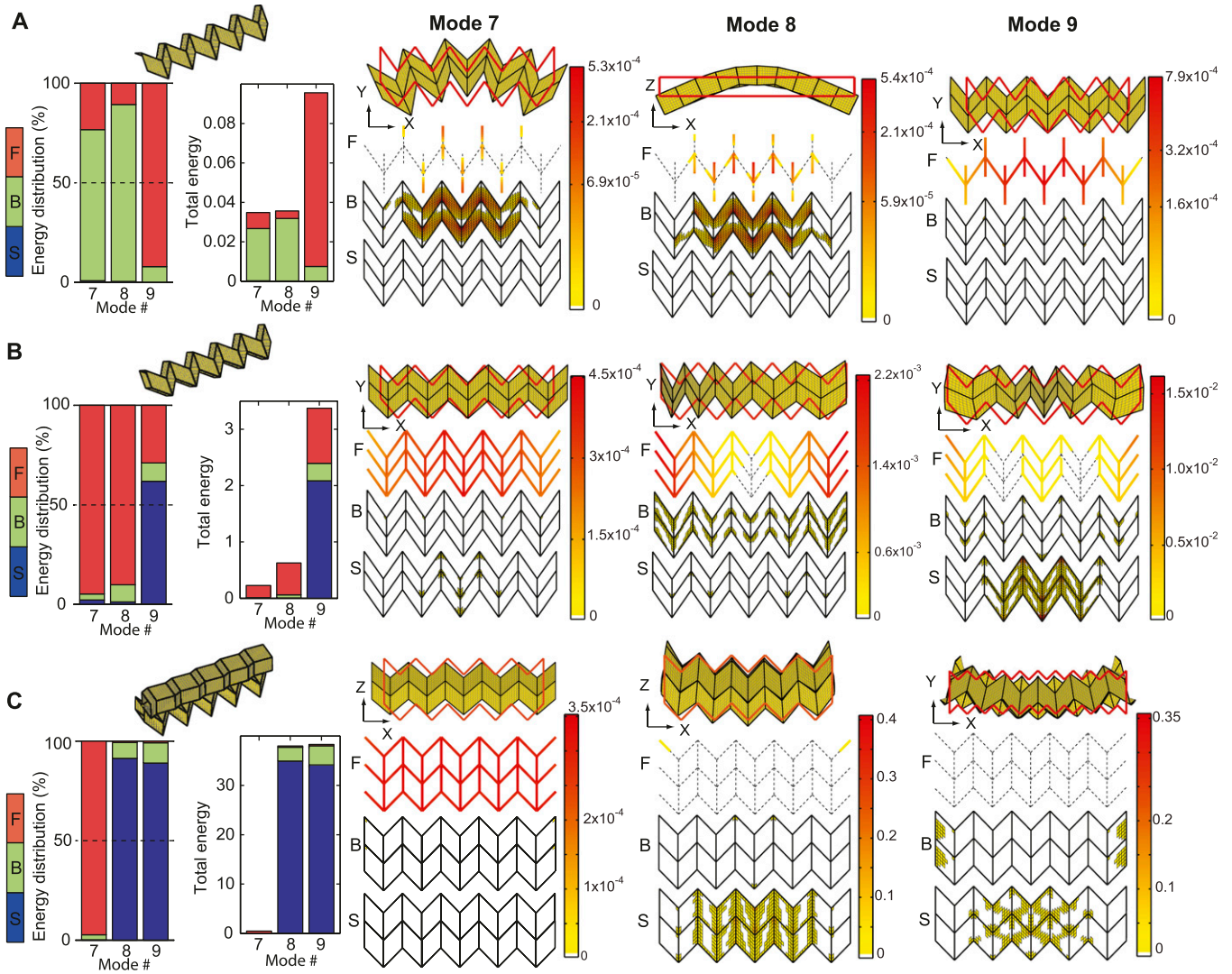


**Fig. S7.** (*A–C*) Eigenmode energies of the sheet, the single tube, and the zipper-coupled tubes, respectively, using FE analysis. Energy distributions (as a percentage and as a total amount) are presented in stacked bar graphs indicating energy in the different sets of components [i.e., fold bending (F), panel bending (B), and panel stretching (S)]. The energy within the structure is shown by shading of elements to show the concentrations of energy. The color scale indicates the magnitude of energy.

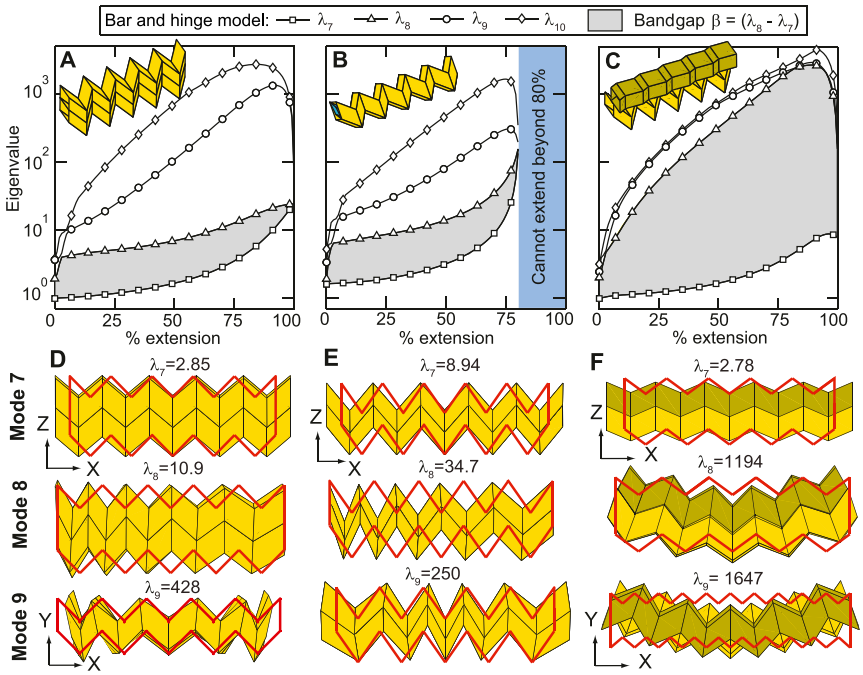


**Fig. S8.** Eigenvalue comparison for the different coupling assemblies. (*A–C*) Eigenvalue vs. extension for the aligned-, internally, and zipper-coupled structures, respectively. (*D–F*) Seventh, eighth, and ninth deformation eigenmodes when structures are at 70% of the maximum extension length (undeformed outline in red).

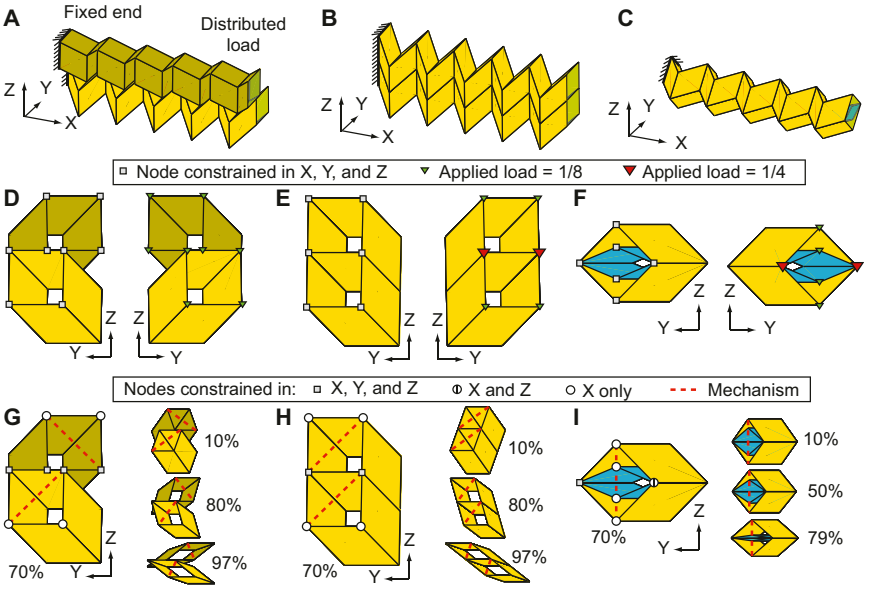


**Fig. S9.** Support and loading conditions of origami cantilever structures. (*A–C*) Initial configurations for the zipper-, aligned-, and internally coupled structures, respectively. (*D–F*) Support conditions (*Left*) and loading conditions (*Right*) used in the analyses of the three cantilever systems in Fig. 4. The total load of 1 is distributed by placing one-eighth of the load at each of the eight nodes, whereas double the load (one-quarter) is placed on colocated nodes occurring in the aligned- and internally coupled systems. (*G–I*) Support conditions (*Left*) for the cantilevers, if a mechanism is installed to deploy the system, and cantilever configurations (*Right*) for different levels of system extensions/contractions.

**Table S1. Geometric definitions and characteristics of coupling variations shown in Figs. 6 and 7**

| Structure | Number and geometries of tubes | Coupling orientation and discussion |
|---|---|---|
| Canopy structure (Fig. 6*A*) | Thirty-two alternating tubes with $\alpha$ varying between 58° and 84°. All tubes with $a=c=0.3$ m and $N=16$. | All tubes are coupled in the zipper orientation. The vertex angles $\alpha$ are calculated so the overall cross section follows a smooth planar curve (e.g., $\alpha=58°, 84°, 60°, 83°, 62°, 82°$ for the first six tubes). This structure covers an area of $8.1\times9.3$ m with a 2.6-m rise when deployed to 97% extension and can fold down to a size of $5.1\times0.8\times$ 1.3 m at 5% extension. |
| Bridge (Fig. 6*B*) | Two tubes with $\alpha=55°$ (yellow) and six with $\alpha=85°$ (green). All tubes with $a=c=25$ mm and $N=5$. | Zipper coupling is continued in one direction only, where each tube is coupled on two opposite faces. The system remains rigid and flat foldable in two directions. The structure has a high out-of-plane stiffness. |
| Self-interlocking structure (Fig. 6*C*) | Twelve tubes with $a=c=25$ mm, $\alpha=75°$, and $N=5$ (red). | Zipper coupling is continued in one direction for each side of the structure. The tubes at the corners have zipper coupling in orthogonal directions (i.e., on two adjacent faces of the tube). The system is flat foldable in one direction and interlocks into a stiff conforming assembly at an extension of 96.3%. |
| Coupled polygonal tube (Fig. 7*A*) | Polygonal tube $N=5$: cross section with four panels of $a=c=25$ mm, $\alpha=55°$ (yellow) and two panels of $a=19$ mm, $c=20$ mm, $\alpha=40.94°$ (blue). One tube has $a=c=25$ mm, $\alpha=55°$ (brown). | Zipper coupling between the polygonal and the regular square tube can be done on any of the polygonal tube faces. The internal (blue) panels of the polygonal tube are defined to reach a flat configuration when external panels (yellow) are at 80% extension. The structure is flat foldable only in one direction, but the internal folds (on blue) can change their polarity and can reconfigure the overall structural shape (Movie S2). |
| Zipper-coupled tubes with thickness (Fig. 7*B*) | Two tubes with $a=80$ mm, $c=40$ mm, $\alpha=75°$, and $N=4$. The thickness is $t=5$ mm on the thin part and $t=10$ mm on the thick part of the panels. | A technique of cutting out material (18) is adopted, allowing the structure to fold down completely to the minimal feasible thickness of $2Nt=80$ mm. The structure cannot extend to 100% extension because intersection of the thick material will occur. |
| Actuator (Fig. 7*C*) | One tube of $N=6$ and one of $N=4$ cells, with $a=c=25$ mm, $\alpha=55°$ (orange). The rigid boundary is a bounded paper box (blue). | Zipper coupling along the middle section of the longer tube, while its ends are adhered to stiff boundaries. The zipper-coupled section prevents local and squeezing-type deformations. At the ends, the longer tube can undergo squeezing, allowing for the rigid attachment. |

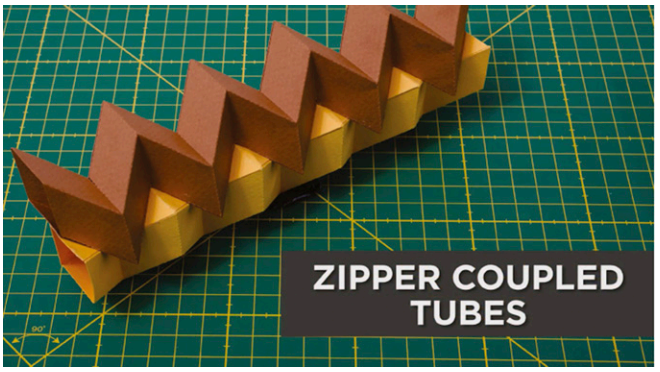


**Movie S1.** Zipper-coupled tubes. Shown are assembly from two single tubes, flat folding, eigenmodes, and system actuation from one end.

Movie S1

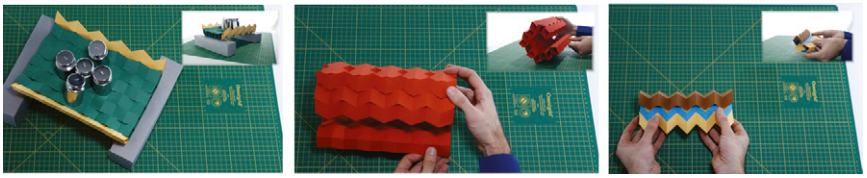

**Movie S2.** Zipper-coupled origami assemblages. Shown are: a bridge structure rigid deployment and loading with 2.5 kg; a self-interlocking structure rigid deployment and interlocking; and a coupled polygonal tube where rigid motion is used to reconfigure the polygonal tube between two different shapes.

Movie S2

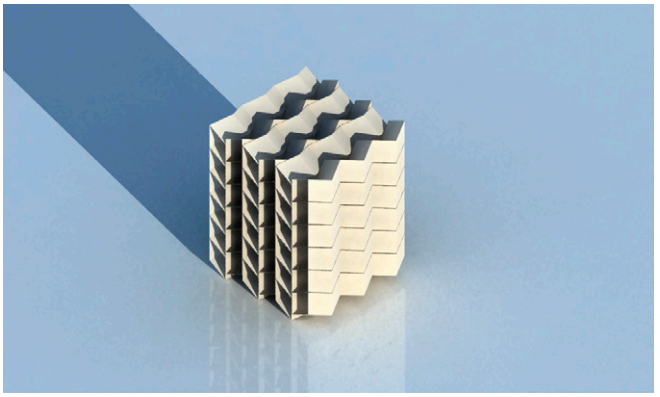

**Movie S3.** Folding sequence of a cellular origami metamaterial consisting of zipper and aligned tubes.

Movie S3

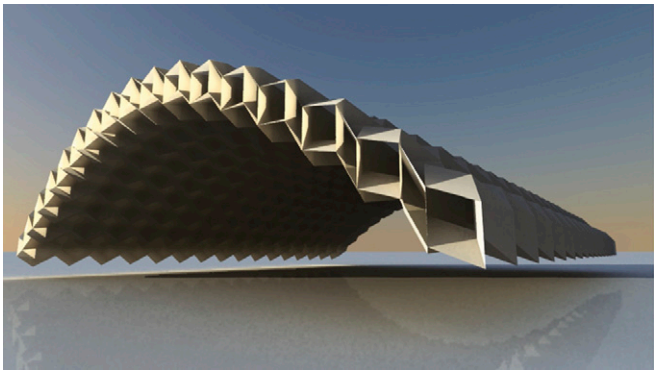

**Movie S4.** Folding sequence of an architectural canopy structure created from geometrically varied zipper-coupled tubes.

Movie S4

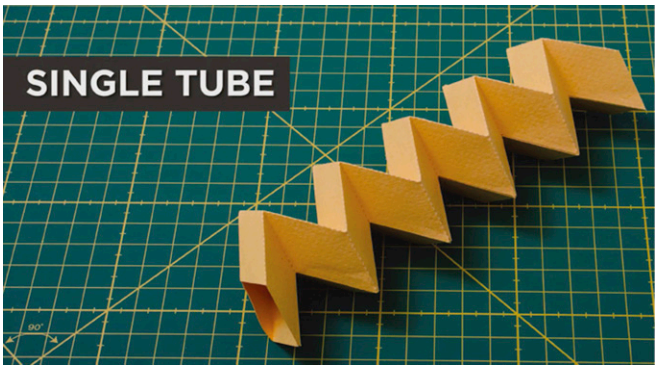


**Movie S5.** Miura-ori sheet and a single tube. Shown are flat folding and eigenmodes of the sheet, assembly of a tube from two sheets, eigenmodes of a tube, and system actuation of the tube from one end.

Movie S5